Acta Metallurgica Sinica (English Letters) (2022) 35:1973–1982
https://doi.org/10.1007/s40195-022-01437-z

Dominant Deformation Mechanisms in Mg–Zn–Ca Alloy

Tao Ying[1] · Mingdi Yu[1] · Yiwen Chen[1] · Huan Zhang[1] · Jingya Wang[1] · Xiaoqin Zeng[1]

Received: 29 March 2022 / Revised: 7 May 2022 / Accepted: 24 May 2022 / Published online: 8 July 2022

Abstract
The coaddition of Zn and Ca has great potential to improve the ductility of Mg alloys. Herein, the mechanical properties of an extruded Mg–Zn–Ca solid-solution alloy were studied by quasi-in situ electron backscatter diffraction (EBSD)-assisted slip trace analysis. The dominant deformation mechanisms of the Mg–Zn–Ca alloy were studied, and the origins of enhanced ductility were systematically revealed. The results indicate that most grains deformed by basal slip. In addition, multiple non-basal slip traces were detected (particularly prismatic, pyramidal I $<a>$, and pyramidal I $<c+a>$ slip traces), and their activation frequency was promoted with increasing tensile strain. The enhanced participation of non-basal slip systems is believed to play a critical role in achieving homogeneous plastic deformation, thus effectively promoting the ductility of the Mg–Zn–Ca alloy. Furthermore, first-principle calculations revealed that the coaddition of Zn and Ca significantly reduces the unstable stacking fault energy for non-basal slip, which contributes to the activation of non-basal slip systems during plastic deformation.

Keywords Mg-Zn-Ca alloy · Non-basal slip activities · First-principle calculations · Generalized stacking fault energy · Deformation mechanisms

1 Introduction

Owing to their low density, high specific stiffness, and superior biodegradability, Mg alloys have great potential for use in the automotive, aerospace, and biomedical industries [1–3]. However, most Mg alloys have low ductility, which reduces their formability and limits their potential applications. Their low ductility originates from their anisotropic hexagonal close-packed (HCP) crystal structure, which has a limited number of available deformation modes. Generally, Mg alloys plastically deform by basal slip and $\{10\bar{1}2\}$ tensile twinning, which possess relatively low activation barriers (represented by the critical resolved shear stress (CRSS)) [4, 5] compared to non-basal slip [6]. Basal slip allows easy deformation along the basal plane, whereas tensile twin occurs when the shear stress specifically favors the extension of the c-axis. However, the number of deformation modes is insufficient to satisfy the von Mises criterion for homogeneous strain, which requires five independent operating systems. Thus, during plastic deformation, Mg alloys accumulate a large amount of strain that is not released homogeneously, resulting in poor ductility.

An effective method of improving the ductility of Mg alloys is to promote alternative deformation modes, such as non-basal slip [7–10] and cross-slip [11]. This can give rise to additional pathways for dislocation motion to accommodate the strain and generate homogeneous plastic deformation. In this regard, reducing the discrepancy in the activation barriers between soft and hard deformation modes is a promising strategy for the design of Mg alloys with complex slip activities and, therefore, high ductility [8]. This has been achieved by the addition of certain solid solution alloying elements, such as Y, Gd, Ca, Li, Ce, and Zn [12–24]. For instance, Zhu et al. [17] reported that the addition of 0.47 wt% Ca to Mg significantly reduces the CRSS discrepancy between pyramidal I $<a>$ and basal $<a>$ slip, which facilitates the activation of non-basal $<a>$ slip, thus leading to enhanced ductility (tensile elongation of approximately 18%). Stanford

✉ Jingya Wang
jingya.wang@sjtu.edu.cn

✉ Xiaoqin Zeng
xqzeng@sjtu.edu.cn

[1] National Engineering Research Center of Light Alloy Net Forming and State Key Laboratory of Metal Matrix Composites, Shanghai Jiao Tong University, Shanghai 200240, China

et al. [24] reported that the addition of Zn to Mg facilitates the participation of prismatic dislocations during plastic deformation on account of the reduced CRSS ratio between prismatic and basal slip.

Recently, an increasing number of researchers have investigated the effect of simultaneous additions of solute Zn and Ca atoms on the mechanical performance of Mg alloys. Mg–Zn–Ca alloys, which can be produced at low cost, reportedly exhibit excellent ductility [25–31]. Kang et al. [26] achieved superior ductility (tensile elongation of 12.3%) and ductile fracture in a Mg–Zn–Ca alloy with the aid of pyramidal $< c + a >$ dislocations. However, the active slip systems were not verified. Zeng et al. [27] observed a larger density of pyramidal II $< c + a >$ slip traces in a rolled Mg–0.3Zn–0.1Ca (wt%) sheet, contributing to appreciably improved ductility (tensile elongation of over 20%). Wang et al. [25] revealed that extensive prismatic slip activities occur during the plastic deformation of Mg–1.8Zn–0.2Ca (wt%) alloy, bestowing the material with excellent ductility. Meanwhile, the tensile twin and pyramidal $< c + a >$ slip activities were identified as inactive.

The influences of Zn and Ca additions on the deformation mechanisms of Mg alloys have been fully investigated via microscale testing [32]. The coexistence of Zn and Ca significantly reduces the CRSS ratio between non-basal and basal slip. This can activate prismatic and pyramidal $< c + a >$ slip and consequently enhance the ductility. From a theoretical perspective, Yuasa et al. [33] predicted through first-principle calculations that the coexistence of Zn and Ca atoms would significantly reduce the stacking fault energy on the prismatic planes, thus promoting basal-to-prismatic cross-slip. However, the dominant deformation mechanisms and crucial factors for high ductility in Mg–Zn–Ca alloys are still under debate on the basis of the abovementioned analyses.

The scope of the present work is to ascertain the deformation mechanisms in Mg–Zn–Ca alloys through experiments and theoretical calculations. The deformation behavior of a Mg–Zn–Ca alloy was studied by using quasi-in situ electron backscatter diffraction (EBSD)-assisted slip trace analysis. The slip activities were identified via slip trace analysis under different deformation strains. With the aim of elucidating the dominant plastic deformation mechanisms and exploring the origins of the improved ductility of the alloy, the deformation behavior was investigated at relatively high tensile strains (8% and 11%). Furthermore, to understand the effect of the coaddition of Zn and Ca on the deformation mechanisms, generalized stacking fault energy (GSFE) curves were calculated via the first-principle calculations for each slip plane in the Mg–Zn–Ca alloy and pure Mg for comparison. The unstable stacking fault energy γ_{us} was determined for the corresponding slip planes as an indicator of the activation barriers of the slip systems [34–36].

2 Methodology

2.1 Experimental Procedures

Commercially pure Mg (99.99%), Zn (99.9%), and Mg–30 wt% Ca master alloys were used to prepare the Mg–Zn–Ca alloy in an electric resistance furnace under a protective atmosphere of CO_2 (99 vol.%) and SF_6 (1 vol.%). The chemical composition of the cast ingot was Mg–1.8Zn–0.067Ca (wt%), as confirmed by inductively coupled plasma atomic emission spectroscopy (ICP-AES). The cast ingots were solution-treated at 400 °C for 12 h followed by extrusion at 300 °C with an extrusion ratio of approximately 18:1.

The microstructure of the extruded alloy was observed using an optical microscope (Zeiss Axioscope 5). The sample was mechanically ground using abrasive SiC papers and electropolished to remove the residual surface damage using a chemical solution of 10 vol.% perchloric acid and 90 vol.% ethanol at − 30 °C and a constant voltage of 30 V. The phase constitution was then analyzed by X-ray diffraction (XRD, D8-advance) in the 2θ scanning range of 10°–90° at a scan speed of 5°/min. The initial extruded texture of the alloy was characterized parallel to the extrusion direction by EBSD using a Tescan GAIA3 (GMU Model 2016) scanning electron microscope (SEM) equipped with an Oxford Instruments Nordlys EBSD detector. The EBSD data were analyzed using Channel 5 software.

Tensile tests were performed to characterize the mechanical properties of the extruded alloy. Tensile specimens with a flat dog-bone shape with a gauge size of 15 mm (length) × 3.5 mm (width) × 2.0 mm (thickness) were machined from the extruded material. The gauge length was parallel to the extrusion direction; therefore, the tensile direction was equivalent to the extrusion direction. Quasi-static tensile tests were conducted at a strain rate of 5×10^{-4} s^{-1} by using quasi-in situ EBSD [37, 38] to probe the slip activity during deformation.

A typical tensile test was performed on a polished specimen and interrupted at strains of 8% and 11% to acquire post-mortem EBSD data and secondary electron (SE) images in the same region. The EBSD data were analyzed using MTEX Toolbox v5.2.8 [39] to identify the orientations of the grains in which slip traces were observed. Simultaneously, the expected traces arising from the slip systems with the highest Schmid factors were predicted by inputting the Euler angles of the corresponding grains into MTEX Toolbox. Then, the assignment of each slip trace to a specific slip system was distinguished by comparing the actual slip traces to those output by the code [37]. Based on this, the activated slip systems were identified.

2.2 First-Principle Calculations

The GSFE curves of each slip system in the Mg–Zn–Ca alloy and pure Mg were calculated via the first-principle calculations using the Vienna ab initio simulation package (VASP) with the Perdew–Burke–Ernzerhof (PBE) functional [40] and projector-augmented wave (PAW) [41] methods. The cutoff energy was set to 480 eV with a Gaussian smearing width of 0.2 eV for geometric relaxation until the electronic energy converged to less than 10^{-4} eV/cell and the Hellmann–Feynman force on all atomic sites was less than 0.01 eV/Å.

Supercells comprising 12 slabs and a total of 48 atoms were established, as shown in Fig. 1. Each slab was separated by a 15 Å vacuum to eliminate artificial interactions. The Brillouin zone for the GSFE of the basal slip system, prismatic slip system, and pyramidal slip system was set as $8\times8\times1$, $10\times6\times1$, and $6\times10\times1$, respectively, with an energy cutoff of 480 eV. To model the solute Zn and Ca atoms in Mg, the cohesive energy was firstly calculated to determine the configurations with different atomic occupancies. The configuration with the lowest cohesive energy was considered stable. In the Mg–Zn–Ca alloy, one solute atom Ca atom was substituted for a Mg atom at the center site of different atomic layers (from the first layer to the sixth layer owing to symmetry). The corresponding cohesive energy was tested to determine the atomic occupancy of Ca. Then, one of the six Mg atoms nearest the Ca atom was substituted with a Zn atom, and the occupancy of Zn was determined based on the lowest cohesive energy. The GSFE curves of each slip system were then calculated by cutting the perfect crystals into two free parts and displacing one part of the crystal along the slip direction within the slip plane. The atomic positions were relaxed along the direction perpendicular to the slip plane.

3 Results

3.1 Microstructure and Mechanical Properties

Figure 2 shows the representative optical micrographs of the Mg–Zn–Ca alloy before and after extrusion. Before extrusion, the solution-treated alloy comprised an α-Mg phase with coarse equiaxed grains, as displayed in Fig. 2a. No precipitates were detected, as confirmed by the XRD pattern (Fig. 3a), which only contained peaks corresponding to the Mg α-phase. Precipitation was suppressed because the alloy composition was within the solution range at the heat treatment temperature of 400 °C, as confirmed by the isopleth section of the Mg–Zn–Ca system (Fig. 4) calculated using Thermo-Calc software. After extrusion, the alloy exhibited a

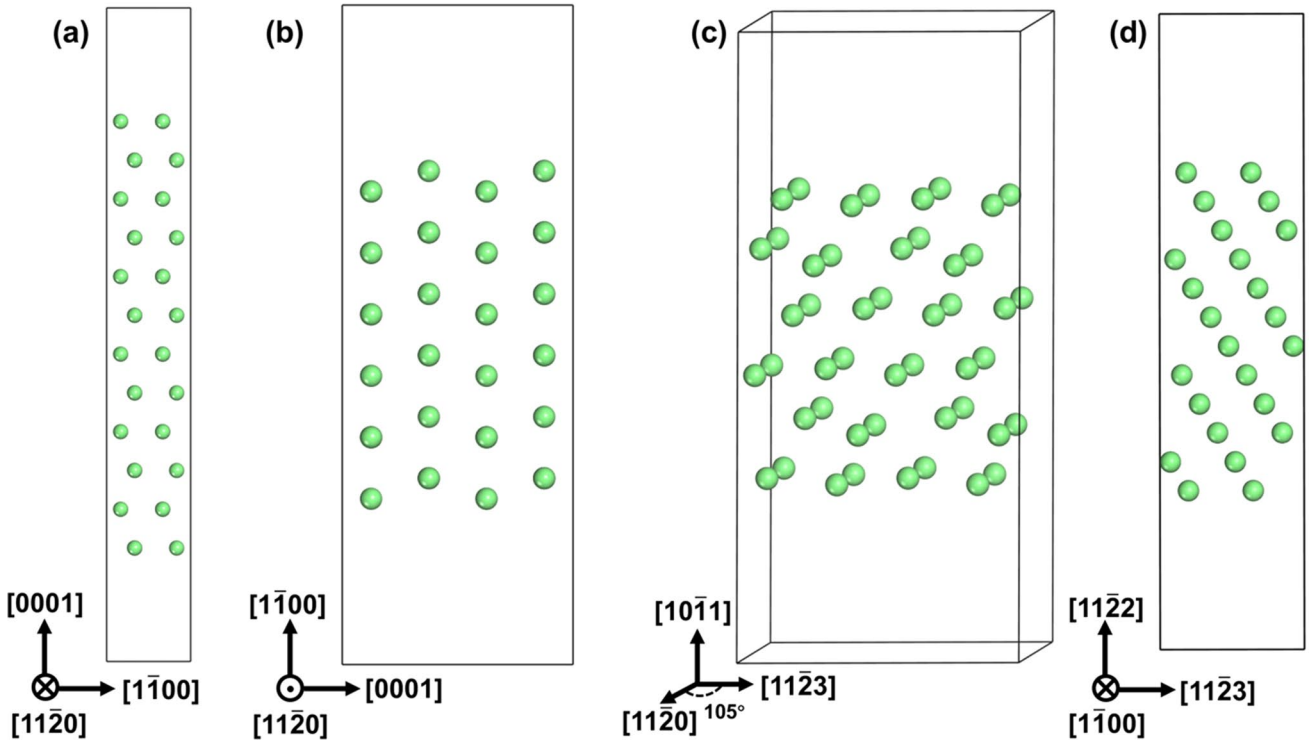

Fig. 1 Schematic illustrations of the supercells used to calculate the GSFE for different slip systems: **a** basal slip plane; **b** prismatic slip plane; **c** pyramidal I slip plane; **d** pyramidal II slip plane

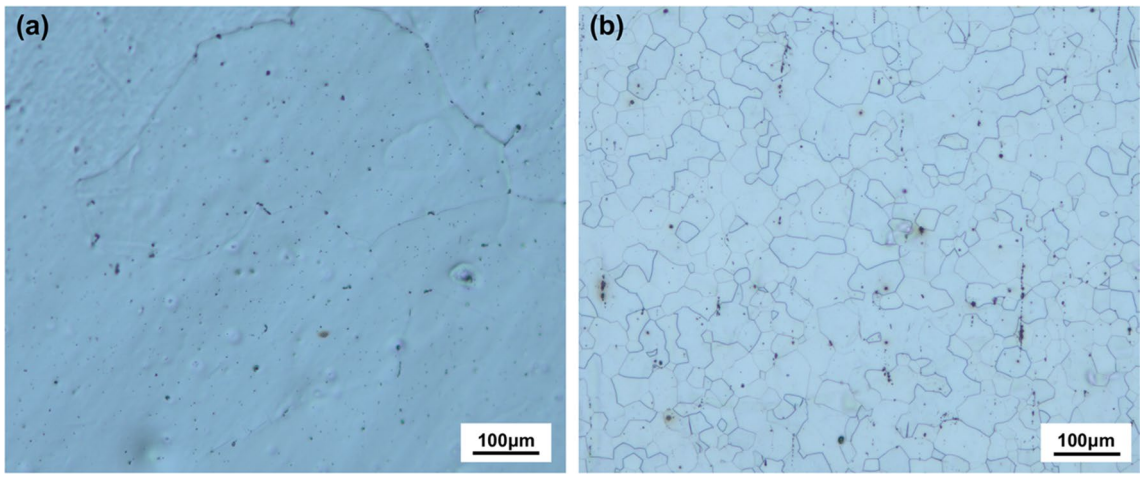

Fig. 2 Optical micrographs of the Mg–Zn–Ca alloy **a** before and **b** after extrusion

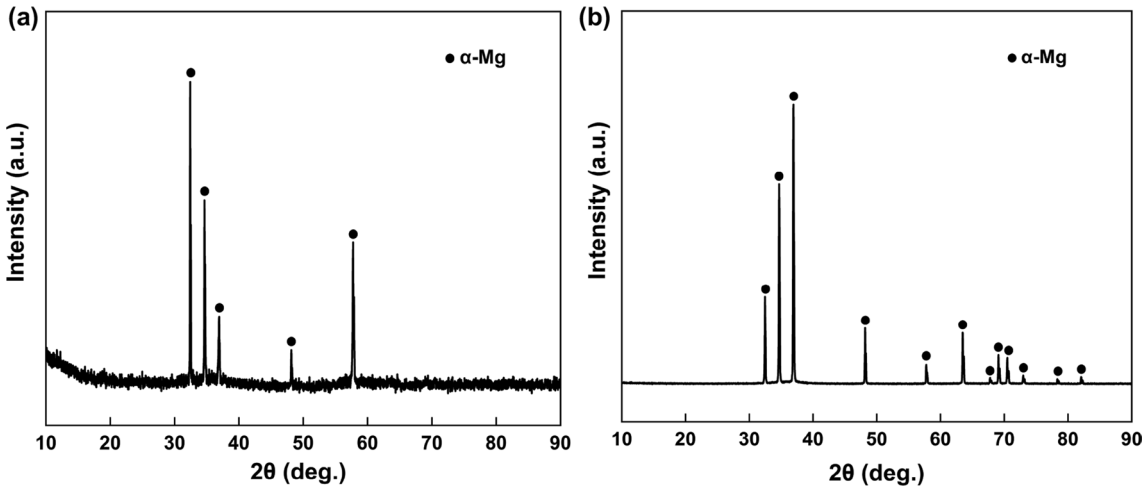

Fig. 3 XRD patterns of the Mg–Zn–Ca alloy **a** before and **b** after extrusion

fully recrystallized microstructure with fine equiaxed grains owing to dynamic recrystallization during the hot extrusion process (Fig. 2b). As the solution-treated alloy, no precipitates were observed in the extruded alloy, as confirmed by XRD result (Fig. 3b). This means the extrusion process has a negligible effect on the phase constitution.

The texture of the extruded alloy was characterized by EBSD. Figure 5a and b shows an inverse pole figure (IPF) map of the alloy and the corresponding pole figures, respectively. The {0001} pole figure displays a typical fiber texture, where the texture intensity is strongest along the transverse direction (TD). This implies that the basal planes preferably approach the TD, which is consistent with the previous results [27, 30]. The texture intensity of ~ 7.9 mrd is weaker than that of pure Mg (~ 18.7 mrd) and a Mg–Zn alloy (~ 12 mrd) [27]. This indicates that the coexistence of Zn and Ca weakens the texture intensity, which is in good agreement with previous work [26, 27]. The grain sizes of the extruded material were randomly distributed (Fig. 5c), with a mean grain size of 27 μm.

Figure 6 shows a representative tensile stress–strain curve of the extruded Mg–Zn–Ca alloy. The yield stress (YS) and ultimate tensile strength (UTS) were determined to be 128 and 211 MPa, respectively. Simultaneously, an excellent ductility was attained with the tensile elongation of approximately 15%, pronouncedly outperforming pure Mg, with a tensile elongation of approximately 3% [27]. The difference between the YS and UTS in the extruded Mg–Zn–Ca alloy was around 83 MPa, which demonstrates that the alloy underwent pronounced strain hardening. This has been extensively reported for Mg–Ca [17] and Mg–Zn–Ca [25] alloys and is thought to originate from the massive slip activities and dislocation interactions during plastic deformation.

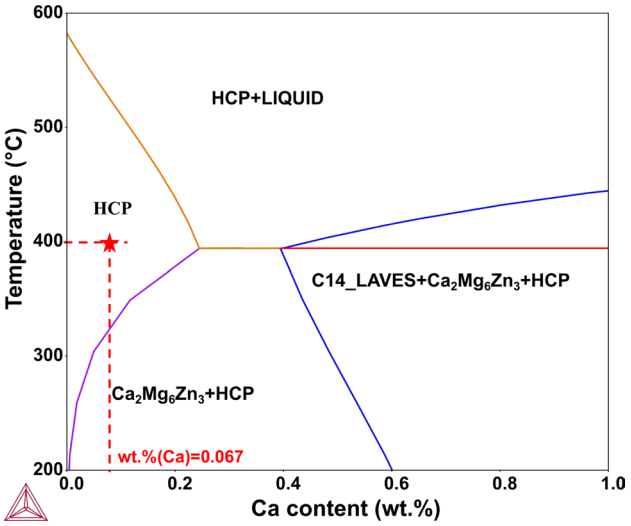

Fig. 4 Isopleth section of the Mg–Zn–Ca system at 1.8 wt% Zn

3.2 Slip Activity Analysis

To ascertain the plastic deformation behavior of the Mg–Zn–Ca alloy, EBSD-assisted slip trace analysis was performed after applying tensile strains of 8% and 11% to identify the dominant deformation modes. Figure 7a shows the EBSD map of the Mg–Zn–Ca alloy after applying 8% tensile strain, with a SEM image presenting the activated slip traces in Fig. 7b and the corresponding {0001} pole figure in Fig. 7c. The texture was consistent with that of the initial extruded microstructure, and the texture intensity remained at ~ 7.9 mrd. This implies that the 8% deformation strain had a negligible influence on the texture.

Slip trace analysis was then conducted within the area of the EBSD analysis. The expected slip traces (corresponding to the intersections of the slip planes and the sample surface) were computed for each grain using MTEX Toolbox by inputting the orientation information. By comparing the theoretically predicted lines with the observed slip traces, the activated slip systems were identified. The slip trace analysis was performed in approximately 200 grains. The analysis results of a partial area are enlarged in Fig. 7b. The activated basal, prismatic, pyramidal I $<a>$, pyramidal I $<c+a>$, and pyramidal II $<c+a>$ slip traces are represented by the red, green, blue, purple, and orange lines, respectively. Among the observed grains, approximately 82 contained the basal slip traces, which dominates the plastic deformation. Indeed, it is normal for the highest activation to be of basal slip, due to the lower CRSS than non-basal slips. In addition, approximately 22 and 12 grains developed the prismatic $<a>$ and pyramidal I $<c+a>$ slips, respectively, while only 2 and 5 grains presented pyramidal I $<a>$ and pyramidal II $<c+a>$ slip traces, respectively.

A tensile strain of 11% was then applied to the same Mg–Zn–Ca alloy specimen. Figure 8 presents the EBSD map of the same area as that in Fig. 7, as well as an SEM image of an enlarged region showing activated slip traces, and the corresponding {0001} pole figure. The texture features were retained as the plastic deformation facilitated. In addition, more slip systems were activated, as shown by the increased number of existed slip traces. Among the observed grains, approximately 117 exhibited traces of the basal slip which remained the dominant deformation mode. Prismatic $<a>$ and pyramidal I $<c+a>$ slip traces were detected in 45 and 25 grains, respectively, demonstrating that these deformation modes were significantly enhanced. Interestingly, pyramidal I $<a>$ slip activation was also markedly promoted, with slip traces observed in 14 grains. In contrast, pyramidal II $<c+a>$ slip activation was still limited, with slip traces observed in only 8 grains. These results indicate that basal slip still plays a dominant role in plastic deformation at 11% strain. However, non-basal slip activity was significantly promoted at higher

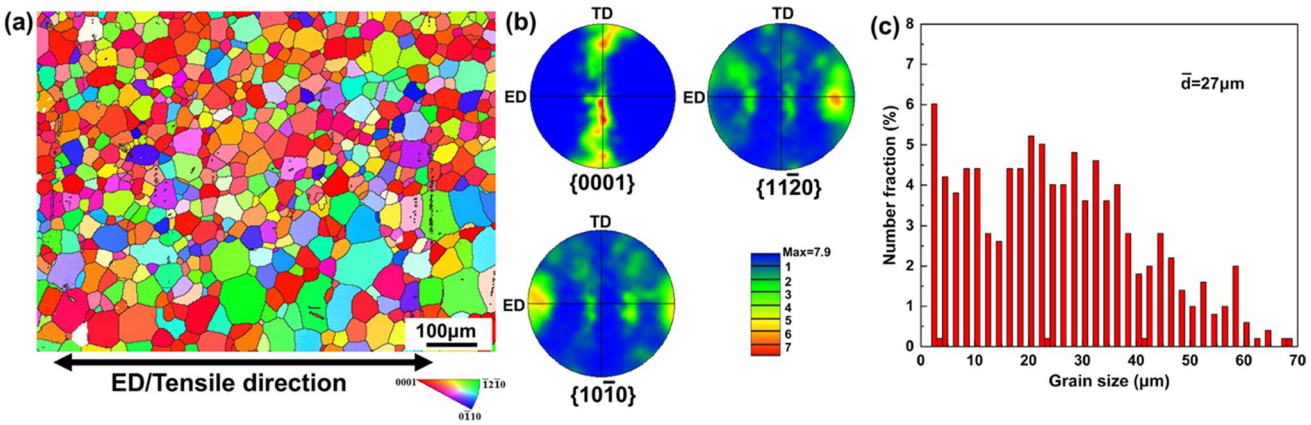

Fig. 5 Microstructures of Mg–Zn–Ca alloy extruded at 300 °C: **a** IPF map; **b** corresponding pole figures; and **c** grain size distribution

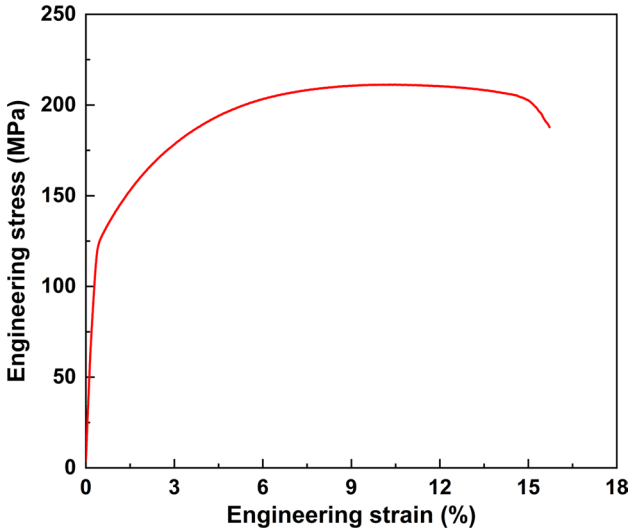

Fig. 6 Representative stress–strain curve of the extruded Mg–Zn–Ca alloy

tensile strains to accommodate the strain. This is beneficial for achieving homogeneous plastic deformation.

It should be noted that tensile twin is generally considered an alternative dominant deformation mode in Mg alloys. Hence, the tensile twin activity was also analyzed. Figure 9a and b shows the boundary misorientation maps of the Mg–Zn–Ca alloy under tensile strains of 8% and 11%, respectively. The $\{10\bar{1}2\}$ tensile twin boundaries are indicated by the red lines and the grain boundaries are marked by black lines. A limited number of grains generated tensile twins during deformation. The twin volume fraction was approximately 1.1% at 8% strain and 1.5% at 11% strain. Thus, tensile twinning has a negligible effect on the deformation behavior, which is consistent with previous work on Mg–Zn–Ca alloys [25, 27].

4 Discussion

4.1 Non-Basal Slip Activity

The identified slip activity at tensile strains of 8% and 11% was statistically analyzed and is summarized in Fig. 10. Owing to its low CRSS, the basal slip accounted for the majority of the slip traces at both strains, with an activity frequency of 66.7% at 8% strain and 56% at 11% strain. The prismatic and pyramidal $I<c+a>$ slip also played a crucial role in plastic deformation, with relatively high activity frequencies of 17.9% and 9.6% at 8% strain, respectively. In contrast, pyramidal $I<a>$ and pyramidal $II<c+a>$ slip only had activity frequencies of 1.6% and 4.2% at 8% strain, respectively. This is significantly different from the slip activity in pure Mg reported by Zheng et al. [42], where 22 of the 24 investigated grains exhibited basal slip under 7% tensile strain, while pyramidal $<c+a>$ slip traces were absent. Evidently, extensive non-basal slip occurred when 8% tensile strain was applied to the Mg–Zn–Ca alloy. As the tensile strain increased to 11%, more grains underwent non-basal slip, with the fractions of prismatic, pyramidal $I<a>$, and pyramidal $I<c+a>$ slips rising to 21.5%, 12%, and 6.7%, respectively. Meanwhile, the activity frequency of pyramidal $II<c+a>$ slip remained at 3.8%, which is comparable to that under 8% strain.

Interestingly, extensive activation of the prismatic slip system occurred during plastic deformation, which is consistent with previous work [25, 32]. Wang et al. [25] reported that the coaddition of solute Zn and Ca atoms enhances the

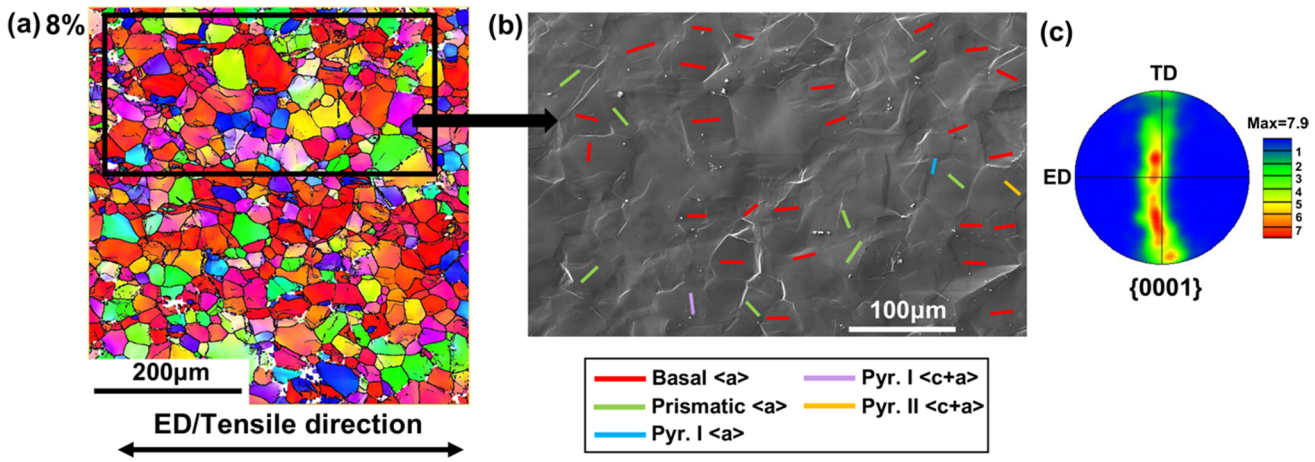

Fig. 7 Slip trace analysis of Mg–Zn–Ca alloy after 8% tensile strain: **a** IPF map; **b** SEM image of part of the deformed region with identified slip traces; **c** corresponding {0001} pole figure. The solid lines represent the relevant slip plane traces with maximum Schmid factors, as simulated by the MTEX Toolbox

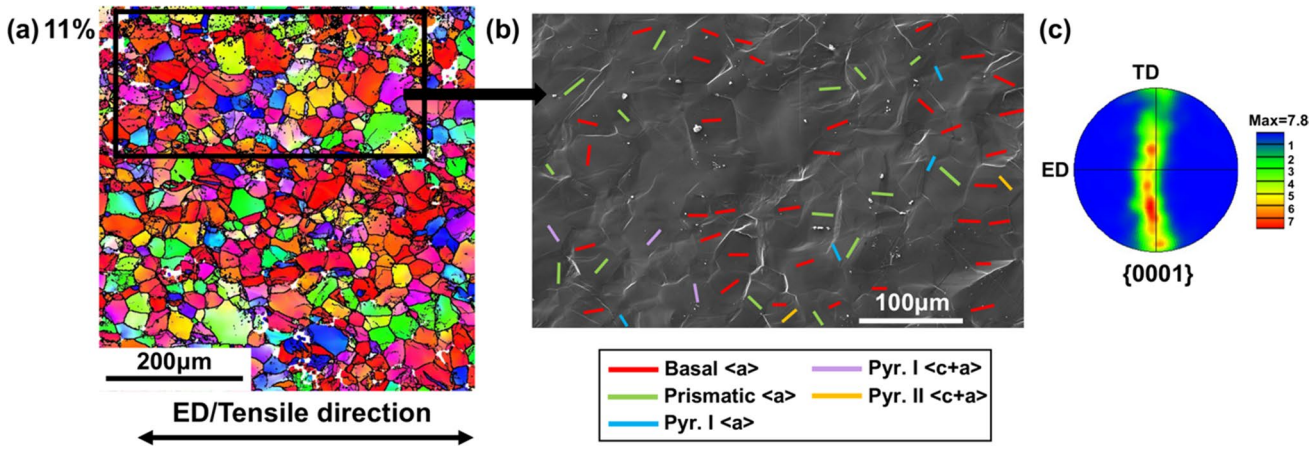

Fig. 8 Slip trace analysis of Mg–Zn–Ca alloy after 11% tensile strain: **a** IPF map; **b** SEM image of part of the deformed region with slip traces; **c** corresponding {0001} pole figure. The solid lines represent the relevant slip plane traces with maximum Schmid factors, as simulated by the MTEX Toolbox

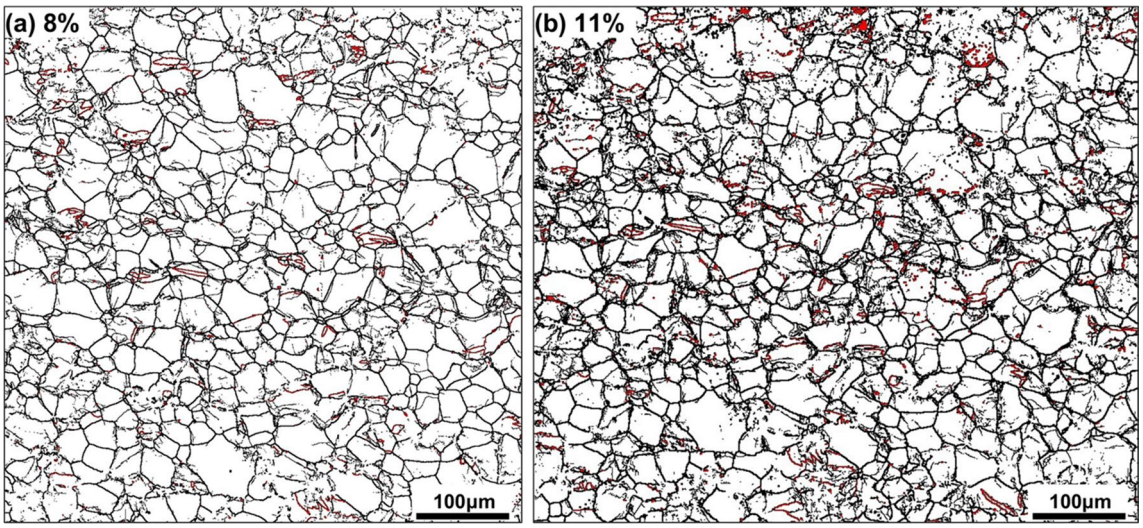

Fig. 9 Boundary misorientation maps of Mg–Zn–Ca alloy deformed under **a** 8% strain and **b** 11% strain. The red and black lines represent $\{10\bar{1}2\}$ tensile twin boundaries and grain boundaries, respectively

activation of prismatic slip relative to that of other slip modes in polycrystalline Mg–Zn–Ca alloys. In addition, prismatic slip activation and cross-slip between the prismatic and basal slip planes have been observed previously in Mg–Zn–Ca alloys subjected to single-crystal micropillar compression tests [32]. As increasing the tensile strain, the pyramidal $I<a>$ slip was gradually activated with the increased activity frequency. This likely originated from the addition of Ca, since extensive pyramidal $I<a>$ slip traces have been found during the plastic deformation of Mg–Ca alloys [17]. Apart from that, the non-basal $<c+a>$ slip increased, especially along the pyramidal I plane, as demonstrated by the higher activity frequency of slip along the pyramidal I plane than the pyramidal II plane. The onset of the non-basal $<c+a>$ slip is mainly attributed to the reduction in CRSS ratio between pyramidal $<c+a>$ and basal slip to approximately 6 [32], ascribed to the coaddition of Zn and Ca. The non-basal $<c+a>$ slip has been extensively observed in polycrystalline Mg–Zn–Ca alloys [26, 27, 43].

The increased activity frequency of non-basal slips reveals that different slip systems are gradually activated as plastic deformation progresses in the Mg–Zn–Ca alloy. The prismatic slip is the preferred non-basal slip owing to the reduced CRSS ratio between prismatic and basal slip [32], followed by the occurrence of pyramidal $I<c+a>$ and $<a>$ slips, as deformation progresses, while

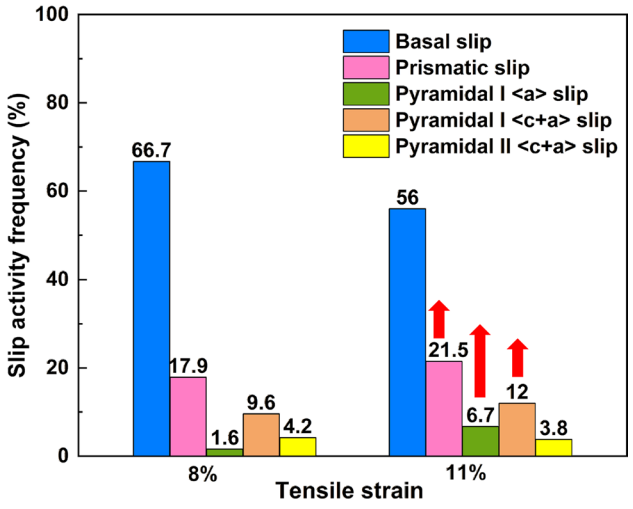

Fig. 10 Frequency of the activated slip systems at different tensile strains for the Mg–Zn–Ca alloy

the activity frequency of pyramidal II $<c+a>$ slip remains consistent as the applied strain increases. Thus, the appearance frequency and activation possibility of the deformation modes follow the trend: basal slip > prismatic slip > pyramidal I $<c+a>$ slip > pyramidal I $<a>$ slip > pyramidal II $<c+a>$ slip.

The multi-activation of non-basal slip systems provides alternative pathways for dislocation motion and potentially improves the ductility of Mg–Zn–Ca alloys. It is worth noting the importance of pyramidal $<c+a>$ slip activity, because $<c+a>$ dislocations are crucial to accommodating strain along the *c*-axis, and therefore achieving more homogeneous plastic deformation. For instance, Pan et al. [43] found a higher density of pyramidal dislocations after the plastic deformation of a Mg–Ca–Al–Zn alloy, which contributed to enhanced ductility. Sandlöbes et al. [19, 44] concluded that $<c+a>$ dislocation activity was responsible for the improved ductility of a Mg–Y alloy, which exhibited a tensile elongation of approximately 25%. Additionally, it is worth noting that quite limited tensile twin occurred during the plastic deformation of the Mg–Zn–Ca alloy, which implied that the twin nucleation was suppressed by the presence of Zn and Ca. This is consistent with previous work [32], which found that the addition of Zn and Ca significantly increased the CRSS for twin growth. The inhibition of tensile twin effectively benefits for the weakened basal texture and contributes to the improved ductility [45]. Therefore, it can be concluded that the prismatic, pyramidal I $<a>$, and pyramidal I $<c+a>$ slip systems are the dominant non-basal plastic deformation modes in the Mg–Zn–Ca alloy. The multi-activation of various slip systems is considered an intrinsically promising strategy to achieve homogeneous plasticity and enhance the ductility of Mg alloys.

4.2 Effect of Alloying Element on the Non-Basal Slip Activity

To ascertain the intrinsic effect of solid solution atoms on slip activity, the GSFE (γ) curves were computed via first-principle calculations for the basal, prismatic, pyramidal I $<a>$, pyramidal I $<c+a>$, and pyramidal II $<c+a>$ slip systems of the Mg–Zn–Ca alloy and pure Mg for comparison. For the Mg–Zn–Ca alloy, the atomic occupancies of the solute atoms were determined preliminarily, as shown in Fig. 11. Two Mg atoms in the sixth atomic layer of the basal plane were substituted by one Zn atom and one Ca atom, as shown in Fig. 11a. Furthermore, the atomic occupancies of the solute Zn and Ca atoms for computing the GSFE curves of the prismatic, pyramidal I, and pyramidal II slip planes are displayed in Fig. 11b-d, respectively.

Figure 12 presents the calculated GSFE curves for all the slip systems in the Mg–Zn–Ca alloy and pure Mg. From the GSFE curves, the unstable stacking fault energy γ_{us} was determined, as shown in Fig. 12. γ_{us} is relevant for estimating the dislocation motion barriers for the slip systems [46]. In the present work, it was employed as an indicator of the activation possibility of the different slip systems.

The addition of Zn and Ca significantly decreased γ_{us} for the basal, prismatic, pyramidal I $<a>$, and pyramidal I $<c+a>$ slip systems. In particular, the γ_{us} value for prismatic slip reduced significantly upon alloying from 323 to 197 mJ/m^2 (Fig. 12b), which is consistent with the results of Yuasa et al. [33]. The reduced activation barrier enhanced the activation of the prismatic slip systems, resulting in the increased activity frequency during plastic deformation. The γ_{us} values for the pyramidal I $<a>$ and $<c+a>$ slip systems decreased upon alloying from 316 to 267 mJ/m^2 and from 267 to 216 mJ/m^2, respectively. This activated the pyramidal I $<a>$ and $<c+a>$ slip systems, producing a high frequency of the corresponding slip traces. In contrast, the γ_{us} value of pyramidal II $<c+a>$ slip increased from 289 mJ/m^2 for pure Mg to 305 mJ/m^2 for the Mg–Zn–Ca alloy. The increased activation barrier for the pyramidal II $<c+a>$ slip explains its limited activity frequency during plastic deformation. Based on the aforementioned analysis, it can be concluded that the presence of Zn and Ca provides an impressive reduction in the activation barriers for non-basal slip systems, particularly for prismatic, pyramidal I $<a>$, and pyramidal I $<c+a>$ slips. This alters the dominant deformation modes during plastic deformation and improves the ductility of the Mg–Zn–Ca alloy.

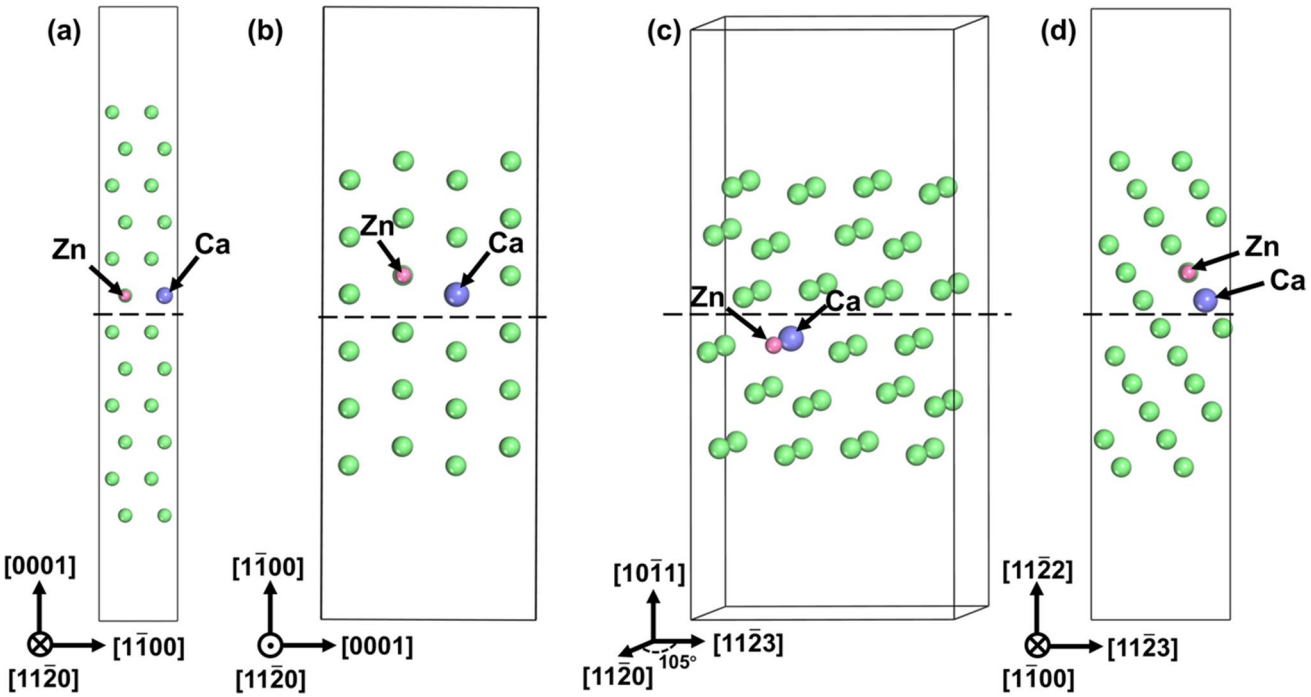

Fig. 11 Schematic models of atomic occupancies in the Mg–Zn–Ca alloy determined by calculating the cohesive energy for different slip systems: **a** basal slip; **b** prismatic slip; **c** pyramidal I slip; and **d** pyramidal II slip

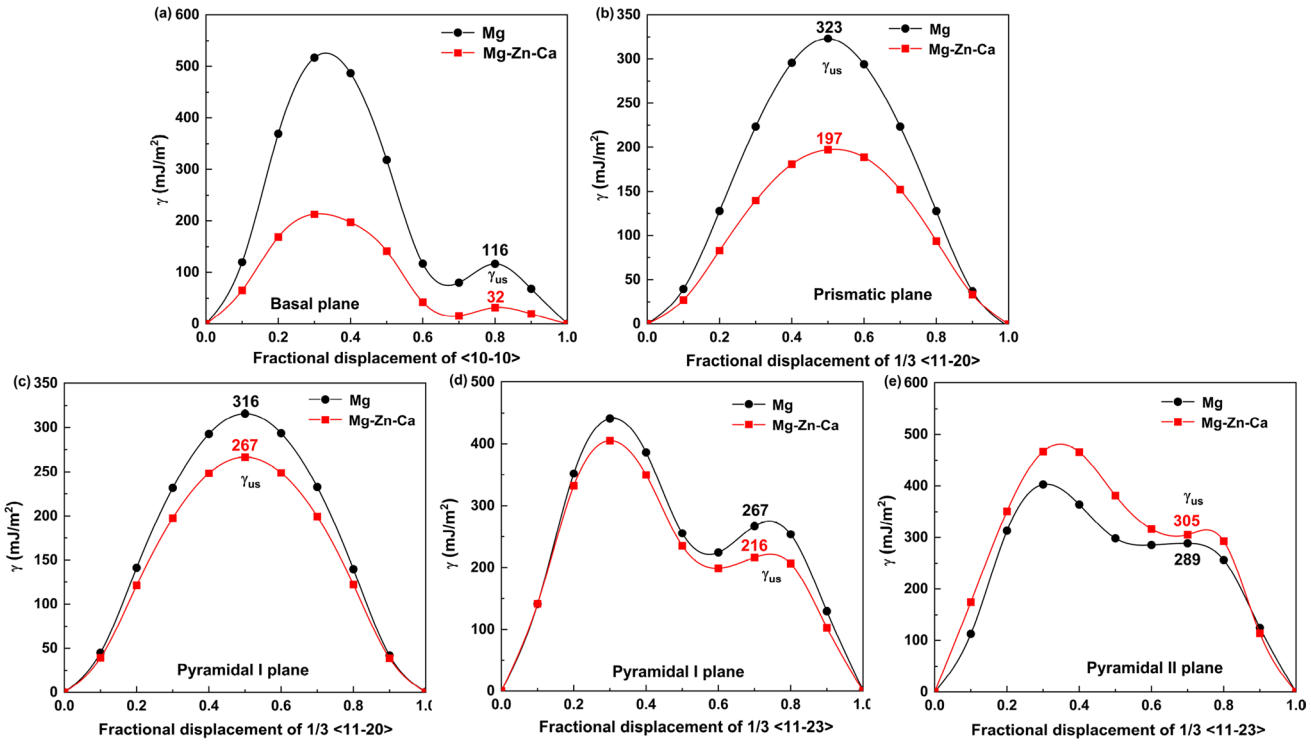

Fig. 12 Calculated GSFE curves for **a** basal slip; **b** prismatic slip; **c** pyramidal I<a>slip; **d** pyramidal I<$c+a$>slip; and **e** pyramidal II<$c+a$>slip

5 Conclusions

The microstructure and mechanical properties of an extruded Mg–Zn–Ca alloy were investigated in this study. The deformation behavior and dominant deformation modes were analyzed via the EBSD-assisted slip trace analysis. Basal slip was the prevalent deformation mode during plastic deformation, with a high activity frequency. In addition, the multi-activation of non-basal slip systems was promoted, with high activity frequencies of the prismatic, pyramidal I $<a>$, and pyramidal I $<c+a>$ slips, conducting the improved ductility of the Mg–Zn–Ca alloy. The effect of alloying elements on the activation of different slip systems was studied using the first-principle calculations. The presence of Zn and Ca significantly reduces the unstable stacking fault energy of the prismatic, pyramidal I $<a>$, and pyramidal I $<c+a>$ slip systems, giving rise to the activation of these slip systems. The enhanced participation of non-basal slip systems plays a critical role in achieving homogeneous plastic deformation, thus effectively promoting the ductility of the Mg–Zn–Ca alloy.

Acknowledgements This work was financially supported by the National Key Research and Development Program of China (No. 2020YFB1505901). X. Zeng and J. Wang acknowledge support from the National Natural Science Foundation of China (Nos. 52001199 and 51825101).

Declarations

Conflict of interests The authors declare that they have no known competing financial interests or personal relationships that could have appeared to influence the work reported in this paper.

References

[1] T.M. Pollock, Science **328**, 986 (2010)
[2] H. Li, J. Wen, Y. Liu, J. He, H. Shi, P. Tian, Adv. Eng. Mater. **22**, 2000213 (2020)
[3] A.A. Luo, JOM **54**, 42 (2002)
[4] H. Yoshinaga, R. Horiuchi, Trans. JIM **4**, 1 (1963)
[5] R.E. Reed-Hill, W.D. Robertson, JOM **9**, 496 (1957)
[6] T. Obara, H. Yoshinga, S. Morozumi, Acta Metall. **21**, 845 (1973)
[7] B.Y. Liu, F. Liu, N. Yang, X.B. Zhai, L. Zhang, Y. Yang, B. Li, J. Li, E. Ma, J.F. Nie, Z.W. Shan, Science **364**, 73 (2019)
[8] G. Liu, J. Zhang, G. Xi, R. Zuo, S. Liu, Acta Mater. **141**, 1 (2017)
[9] H. Somekawa, M. Yamaguchi, Y. Osawa, A. Singh, M. Itakura, T. Tsuru, T. Mukai, Philos. Mag. **95**, 869 (2015)
[10] R. Ahmad, B. Yin, Z. Wu, W.A. Curtin, Acta Mater. **172**, 161 (2019)
[11] Z. Wu, R. Ahmad, B. Yin, S. Sandlöbes, W.A. Curtin, Science **359**, 447 (2018)
[12] R.K. Sabat, A.P. Brahme, R.K. Mishra, K. Inal, S. Suwas, Acta Mater. **161**, 246 (2018)
[13] S. Sandlöbes, Z. Pei, M. Friák, L.F. Zhu, F. Wang, S. Zaefferer, D. Raabe, J. Neugebauer, Acta Mater. **70**, 92 (2014)
[14] W.B. Hutchinson, M.R. Barnett, Scr. Mater. **63**, 737 (2010)
[15] J. Yang, J. Peng, M. Li, E.A. Nyberg, F.S. Pan, Acta Metall. Sin. -Engl. Lett. **30**, 53 (2017)
[16] F.W. Jiao, L. Jin, J. Dong, F.H. Wang, Acta Metall. Sin. Engl. Lett. **32**, 263 (2019)
[17] G. Zhu, L. Wang, H. Zhou, J. Wang, Y. Shen, P. Tu, H. Zhu, W. Liu, P. Jin, X. Zeng, Int. J. Plast. **120**, 164 (2019)
[18] S.R. Agnew, J.A. Horton, M.H. Yoo, Metall. Mater. Trans. A **33**, 851 (2002)
[19] S. Sandlöbes, M. Friák, S. Zaefferer, A. Dick, S. Yi, D. Letzig, Z. Pei, L.F. Zhu, J. Neugebauer, D. Raabe, Acta Mater. **60**, 3011 (2012)
[20] Y. Chino, M. Kado, M. Mabuchi, Mater. Sci. Eng. A **494**, 343 (2008)
[21] S. Sandlöbes, M. Friák, J. Neugebauer, D. Raabe, Mater. Sci. Eng. A **576**, 61 (2013)
[22] L. Wang, Z. Huang, H. Wang, A. Maldar, S. Yi, J.S. Park, P. Kenesei, E. Lilleodden, X. Zeng, Acta Mater. **155**, 138 (2018)
[23] A. Akhtar, E. Teghtsoonian, Acta Metall. **17**, 1351 (1969)
[24] N. Stanford, M.R. Barnett, Int. J. Plast. **47**, 165 (2013)
[25] J. Wang, G. Zhu, L. Wang, E. Vasilev, J.-S. Park, G. Sha, X. Zeng, M. Knezevic, J. Mater. Sci. Technol. **84**, 27 (2021)
[26] Q. Kang, H. Jiang, Y. Zhang, Z. Xu, H. Li, Z. Xia, J. Alloy. Compd. **742**, 1019 (2018)
[27] Z.R. Zeng, M.Z. Bian, S.W. Xu, C.H.J. Davies, N. Birbilis, J.F. Nie, Mater. Sci. Eng. A **674**, 459 (2016)
[28] J. Hofstetter, S. Rüedi, I. Baumgartner, H. Kilian, B. Mingler, E. Povoden-Karadeniz, S. Pogatscher, P.J. Uggowitzer, J.F. Löffler, Acta Mater. **98**, 423 (2015)
[29] K.B. Nie, Z.H. Zhu, P. Munroe, K.K. Deng, J.G. Han, Acta Metall. Sin. -Engl. Lett. **33**, 922 (2020)
[30] J. Luo, H. Yan, N. Zheng, R.S. Chen, Acta Metall. Sin. -Engl. Lett. **29**, 205 (2016)
[31] T. Tu, X.H. Chen, J. Chen, C.Y. Zhao, F.S. Pan, Acta Metall. Sin. -Engl. Lett. **32**, 23 (2019)
[32] J. Wang, Y. Chen, Z. Chen, J. Llorca, X. Zeng, Acta Mater. **217**, 117151 (2021)
[33] M. Yuasa, M. Hayashi, M. Mabuchi, Y. Chino, Acta Mater. **65**, 207 (2014)
[34] J.A. Yan, C.Y. Wang, S.Y. Wang, *Phys* (B - Condens. Matter Mater. Phys, Rev, 2004). https://doi.org/10.1103/PhysRevB.70.014402
[35] A.A. Kaya, Front. Mater. **7**, 1 (2020)
[36] J.A. Yasi, L.G. Hector, D.R. Trinkle, Acta Mater. **58**, 5704 (2010)
[37] J.L. Li, D. Wu, R.S. Chen, E.H. Han, Acta Mater. **159**, 31 (2018)
[38] C.M. Cepeda-Jiménez, J.M. Molina-Aldareguia, M.T. Péez-Prado, Acta Mater. **84**, 443 (2015)
[39] F. Bachmann, R. Hielscher, H. Schaeben, Solid State Phenom. **160**, 63 (2010)
[40] J.P.J. Perdew, K. Burke, M. Ernzerhof, Phys. Rev. Lett. **77**, 3865 (1996)
[41] P.E. Blöchl, Phys. Rev. B **50**, 17953 (1994)
[42] T. Zheng, Y. Hu, C. Zhang, T. Zhao, F. Pan, A. Tang, Mater. Charact. **179**, 111299 (2021)
[43] H. Pan, R. Kang, J. Li, H. Xie, Z. Zeng, Q. Huang, C. Yang, Y. Ren, G. Qin, Acta Mater. **186**, 278 (2020)
[44] S. Sandlöbes, S. Zaefferer, I. Schestakow, S. Yi, R. Gonzalez-Martinez, Acta Mater. **59**, 429 (2011)
[45] S.R. Agnew, M.H. Yoo, C.N. Tomé, Acta Mater. **49**, 4277 (2001)
[46] A. Tehranchi, B. Yin, W.A. Curtin, Acta Mater. **151**, 56 (2018)